Entrainment in a Simulated Supercell Thunderstorm. Part II: The Influence of Vertical Wind Shear and General Effects upon Precipitation

ENOCH JO[a] AND SONIA LASHER-TRAPP[a]

[a] *University of Illinois at Urbana–Champaign, Urbana, Illinois*

(Manuscript received 27 October 2021, in final form 20 January 2022)

ABSTRACT: Supercell thunderstorms can produce heavy precipitation, and an improved understanding of entrainment may help to explain why. In Part I of this series, various mechanisms of entrainment were identified in the rotating stage of a single simulated supercell thunderstorm. The current study examines the strength and effectiveness of these mechanisms as a function of the environmental vertical wind shear in eight different supercell simulations. Entrainment is calculated directly as fluxes of air over the surface of the storm core; tracers are used to assess the resulting dilution of the moistest air ingested by the storm. Model microphysical rates are used to compare the impacts of entrainment on the efficiency of condensation/deposition of water vapor on hydrometeors within the core, and ultimately, upon precipitation production. Results show that the ascending "ribbons" of horizontal vorticity wrapping around the updraft contribute more to entrainment with increasing vertical wind shear, while turbulent eddies on the opposite side of the updraft contribute less. The storm-relative airstream introduces more low-level air into the storm core with increasing vertical wind shear. Thus, the total entrainment increases with increasing vertical wind shear, but the fractional entrainment decreases, yielding an increase in undiluted air within the storm core. As a result, the condensation efficiency within the storm core also increases with increasing vertical wind shear. Due to the increase in hydrometeors detrained aloft and the resulting enhanced evaporation as they fall, the precipitation efficiency evaluated using surface rainfall decreases with increasing vertical wind shear, as found in past studies.

KEYWORDS: Entrainment; Supercells; Cloud microphysics

1. Introduction

The effects of entrainment upon the precipitation production of a supercell storm are yet to be established; such understanding is of major importance to improving precipitation forecasts to mitigate losses of life and property from short-term severe weather events (Doswell et al. 1996). Over longer periods, a better understanding of entrainment also has the potential to improve estimates of cloud cover, cloud radiative forcings, and storm longevity in large-scale climate models (Rio et al. 2019; Sui et al. 2020).

Older numerical studies of supercell thunderstorms lacked the spatial resolution to investigate entrainment in detail (e.g., Rotunno and Klemp 1985; James and Markowski 2010) and thus tended to only refer to evaporation effects upon precipitation development. Historically, precipitation production has been gauged within deep convective storms using the so-called precipitation efficiency, the ratio between the masses of the surface precipitation produced by a storm and the water vapor the storm ingested (e.g., Braham 1952; Doswell et al. 1996). Although the exact definition or method of calculating precipitation efficiency varies, its relationship to increasing vertical wind shear for isolated thunderstorms is generally negative (Marwitz 1972; Fritsch and Chappell 1980; Market et al. 2003). Supercell thunderstorms, on the higher end of the vertical wind shear spectrum, were noted to be among the least efficient at converting water vapor to surface precipitation despite being associated with some of the heaviest rainfall, with precipitation efficiency ranging from 5% to 20% (Auer and Marwitz 1968; Marwitz 1972; Foote and Fankhauser 1973). These low efficiency values were attributed to "erosive" processes near the storm boundaries, where strong environmental winds aloft were hypothesized to remove cloud condensate through the evaporation of cloud droplets caused by the impingement of dry air (e.g., Grant and Van Den Heever 2014), and also through the downwind transport of hydrometeors near the storm top (i.e., anvils), allowing more depth over which falling precipitation could evaporate and/or sublimate before reaching the surface (e.g., Newton 1963; Marwitz 1972; Foote and Fankhauser 1973). Nonetheless, overall trends in supercell precipitation efficiency as a function of the environmental vertical wind shear have not been explicitly addressed, likely due to the complex interplay of multiple factors that can also influence precipitation at the ground (e.g., entrainment, transport of hydrometeors by the rotating updraft, evaporation of falling hydrometeors), requiring new ways to examine these trends.

Part I of this series (Lasher-Trapp et al. 2021, hereafter LT21) discussed the evolution of entrainment mechanisms and their dilutive effects on a single numerically simulated supercell thunderstorm. In the mature stage of the supercell when a strong rotating updraft was present, the greatest local entrainment rates resulted from a mechanism first

Denotes content that is immediately available upon publication as open access.

Supplemental information related to this paper is available at the Journals Online website: https://doi.org/10.1175/JAS-D-21-0289.s1.

Corresponding author: Enoch Jo, enochjo2@illinois.edu

DOI: 10.1175/JAS-D-21-0289.1

identified in LT21: overturning "ribbons" of horizontal vorticity at the edge of the updraft core, hypothesized to be generated through horizontal buoyancy gradients, and observed to be most prominent on the side of the core where the cyclonic flow of the mesocyclone worked in tandem with the environmental winds, amplifying the ribbons by stretching their vorticity. On the opposite side of the core, where the cyclonic flow of the mesocyclone was opposed to the environmental winds, disorganized turbulent eddies entrained some air into the core, but in lower amounts. LT21 also identified another entrainment mechanism that they called the "storm-relative airstream," referring to the air streaming diagonally into the downshear side of the core from above the LCL. This mechanism was considered to be separate from the vertical mass flux of warmer and moister air from below the LCL into the storm base, due to the different thermodynamic properties of that air. Within the storm core, the air entrained from the storm-relative airstream was often separate from the air entering beneath the core base, but sometimes could be diluted by the ribbons and entraining disorganized eddies.

Due to the use of a single simulation, LT21 was unable to investigate how these various entrainment mechanisms might differ for supercells in other environments with different amounts of vertical wind shear. As in the tilting of horizontal shear vorticity to create midlevel vertical rotation (e.g., Barnes 1970; Wilhelmson and Klemp 1978; Davies-Jones 1984; Rotunno and Klemp 1985), it is possible that with increasing environmental vertical wind shear, increased stretching of the horizontal vorticity of the ribbons might amplify their entrainment. The storm-relative airstream should also change with the vertical wind shear of the environment; supercells existing in highly sheared environments are associated with faster translation speeds (e.g., Bunkers et al. 2000), stronger storm-relative environmental winds, and stronger storm inflow (e.g., Warren et al. 2017)—the latter of which partially owes its source to a more deviant storm motion relative to the mean flow (Rotunno and Klemp 1982, 1985; Davies-Jones 2002). Thus, the contribution of the entraining storm-relative airstream to the storm buoyancy and precipitation production should vary with the strength of the environmental wind shear.

Fractional entrainment, the horizontal mass flux from entrainment normalized by the vertical mass flux in the updraft, can indicate potential trends in dilution across different clouds and storms (e.g., Morton et al. 1956; Turner 1963), but does not provide details about how that dilution occurs. Peters et al. (2020) found that the fractional entrainment of simulated nonsupercell storms was larger than that of simulated supercell storms. Previous studies showed positive correlations between supercell updraft width and vertical wind shear (e.g., Kirkpatrick et al. 2009; Warren et al. 2017; Trapp et al. 2017; Marion and Trapp 2019; Peters et al. 2019) and an inverse trend of fractional entrainment to increasing storm radius (e.g., Squires and Turner 1962; Simpson et al. 1965; De Rooy et al. 2013; Hernandez-Deckers and Sherwood 2018), thus supporting the conclusion of Peters et al. (2020) that dilution decreases in supercells with increasing environmental wind shear due to an increasing updraft width. LT21 found a similar value of fractional entrainment in their simulation to those of Peters et al. (2020), but also identified the individual contributions of different entrainment mechanisms to the dilution of the core. Overall, LT21 found that approximately 20% of the storm core contained undiluted air from beneath the LCL as well as undiluted air entrained above it by the storm-relative airstream, but speculated that the dilution might adapt to variations in environmental wind shear owing to changes in the individual entrainment mechanisms themselves.

It is the purpose of Part II of this series of papers on entrainment in supercell thunderstorms to clarify the relationships between the environmental vertical wind shear to the strength of various entrainment mechanisms found in Part I (LT21), and to evaluate the resulting impacts of the entrainment upon dilution of the supercell core, and upon precipitation production. Here, multiple idealized, high-resolution simulations of supercells in environments differing only in their amount of vertical wind shear are analyzed. The methods used to calculate entrainment, isolate specific entrainment mechanisms, and quantify their effects on dilution and precipitation production are introduced in section 2, and results are presented in section 3 within the overall themes of entrainment, dilution, and precipitation efficiency. Conclusions and additional discussion are presented in section 4.

2. Methods

a. The model

Idealized supercell simulations are produced with Cloud Model 1 (CM1), v19.6 (Bryan and Fritsch 2002), configured to integrate the fully compressible, three-dimensional Navier–Stokes equations with rigid top and bottom and open-radiative lateral boundaries. CM1 is configured to use the Arakawa C grid with scalars on the center and the velocities on the surfaces of each grid box. Sixth-order horizontal and vertical advection schemes are used for velocities with added artificial diffusion for stability. The fully explicit Klemp–Wilhelmson time-splitting method (Klemp and Wilhelmson 1978) is used for temporally integrating pressure to control for acoustic waves in the model domain with equal 100-m grid spacings in the horizontal and vertical directions to resolve turbulent eddies of similar sizes in all directions (Bryan et al. 2003; Petch 2006; Lebo and Morrison 2015). The fifth-order weighted essentially nonoscillatory (WENO) scalar advection scheme (Jiang and Shu 1996) is preferred for better integration with the NSSL microphysics scheme (Mansell et al. 2010; Mansell and Ziegler 2013), which represents both rimed ice categories (graupel and hail), an important consideration when simulating supercells. Vertical motion is introduced within the initial horizontally homogeneous environment via a Gaussian surface heating function (Carpenter et al. 1998) as also used by LT21.

b. The simulations

The environmental soundings of the simulations are designed to produce strong supercell updrafts capable of sustained convection for over 30 min. All simulations are

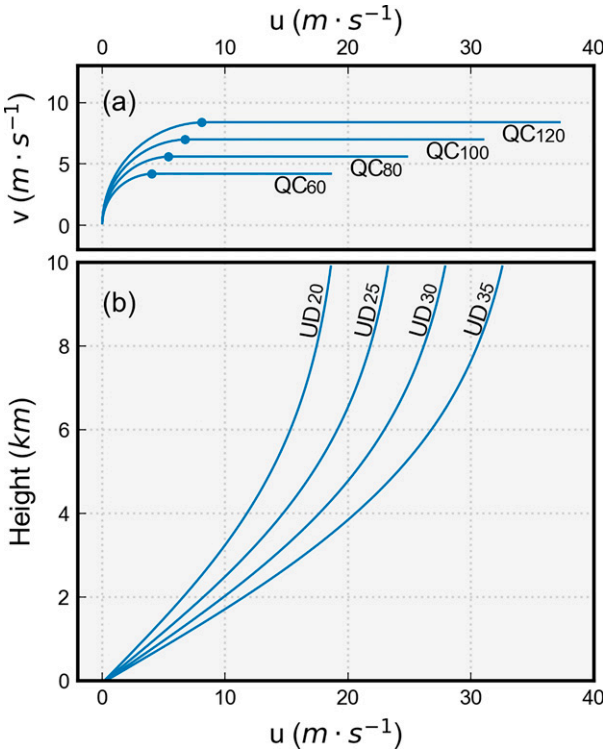

FIG. 1. (a) Quarter-circle hodographs of the simulations including directional and speed vertical wind shear, as labeled, with dots corresponding to values at 2 km AGL height. Ends of the hodographs correspond to wind speeds at 6 km AGL height and above. (b) Vertical wind profiles for the unidirectional shear simulations, as labeled.

initialized with the idealized thermodynamic sounding of Weisman and Klemp (1982) with a mixed layer water vapor mixing ratio of 14 g kg^{-1}, identical to that used by LT21 (cf. their Fig. 1). The LCL of a surface-based parcel is located at 1.2 km AGL and the CAPE of this parcel is 2000 J kg^{-1}. Eight simulations are examined in this study with systematic variations in the environmental vertical wind profiles. Four simulations employ variations of the quarter circle (QC) hodograph used by Weisman and Rotunno (2000) (Fig. 1a), where only the wind speeds of the QC simulations are varied—by 60% (QC60), 80% (QC80), 100% (QC100), and 120% (QC120) of the original vertical wind profile, with respective 0–6-km bulk wind shear values ranging from 18.9 to 37.8 m s^{-1}. The four unidirectional wind profiles follow Weisman and Klemp (1982), where the majority of vertical wind shear is modified to occur in the lowest 6 km of the atmosphere (Fig. 1b). These simulations range from maximum wind speeds of 20 (UD20) to 35 m s^{-1} (UD35) with respective 0–6-km bulk wind shear ranging from 15.2 to 26.5 m s^{-1}. As in LT21, the modified Pearson coefficient (Naylor et al. 2012) is used to quantify the correlation between vertical updrafts and positive vertical vorticity, to objectively determine that the storms analyzed were supercells with rotating updrafts.

As in LT21, the vertical wind profiles used in the model are not modified by subtracting a constant wind speed to keep the storm centered in the domain, because it would alter the entrainment results on different sides of the storms. Thus, large domains are required to contain the storms during the extent of the simulations. Seven out of the eight runs utilize domains of horizontal dimensions 160 km × 80 km. The QC120 supercell, which had the fastest storm translation speed, required a larger domain, 176 km × 100 km.

c. *Quantifying entrainment*

The method employed by LT21 for the direct calculation of entrainment is also used here, adapted from Dawe and Austin (2011). However, unlike LT21, entrainment is calculated only during the mature stage of the storm, to address the relative lack of studies on the entrainment characteristics of mature, cyclonically rotating supercells in the literature. The core is defined by the largest contiguous volume of updraft that exceeds 20 m s^{-1}. Experimentation with higher and lower thresholds to define the core showed this value was an optimal compromise: a higher threshold can force the entrainment values near zero as the core surface reaches the undiluted core, and a lower threshold can cause the main updraft to intermittently detach and reattach to surrounding smaller "chunks" of updraft, yielding unstable core surfaces that make entrainment values noisy. LT21 also considered the total hydrometeor mixing ratio to define the core, but it is no longer considered as a constraint on the supercell core here, to allow further evaluation of the effects of entrainment-driven evaporation and sublimation of hydrometeor species near the core boundaries. To increase the accuracy of entrainment across the core surface, the algorithm divides each model grid box into 48 tetrahedrons and linearly interpolates to approximate the subgrid core boundaries. Entrainment and detrainment are calculated on this interpolated surface (see the animated Fig. S1 of the online supplement) by combining instantaneous fluxes of air through the core and changes in core volume with time [dV/dt; cf. Eq. (13) in Dawe and Austin 2011].

Large storage requirements associated with running eight separate simulations in this study necessitated increasing the model output interval from the 6 s used in LT21 to 15 s. This modification, however, is accompanied by a complication: the dV/dt term, which accounts for the translation and the expansion/contraction of the core surface, requires high temporal resolution in model output, and can be most accurately assessed if the leading edge of the core surface does not move beyond one grid space (here, 100 m) within a single output interval. As a workaround, entrainment is now evaluated using Eq. (1) within a storm-relative framework:

$$
\begin{aligned}
E - D = {} & \rho_{(k)}\left[\frac{dV_{(i,j,k)}}{dt}\right]^{*} \\
& + \rho_{(k)}u^{*}_{(i+1,j,k)}W_{x(i+1,j,k)} - \rho_{(k)}u^{*}_{(i,j,k)}W_{x(i,j,k)} \\
& + \rho_{(k)}v^{*}_{(i,j+1,k)}W_{y(i,j+1,k)} - \rho_{(k)}v^{*}_{(i,j,k)}W_{y(i,j,k)} \\
& + \frac{1}{2}\left[\rho_{(k)} + \rho_{(k+1)}\right]w_{(i,j,k+1)}W_{z(i,j,k+1)} \\
& + \frac{1}{2}\left[\rho_{(k)} + \rho_{(k-1)}\right]w_{(i,j,k-1)}W_{z(i,j,k-1)}, \qquad (1)
\end{aligned}
$$

where dV/dt now only represents the expansion or contraction of the storm core volume, and no longer includes the effect of

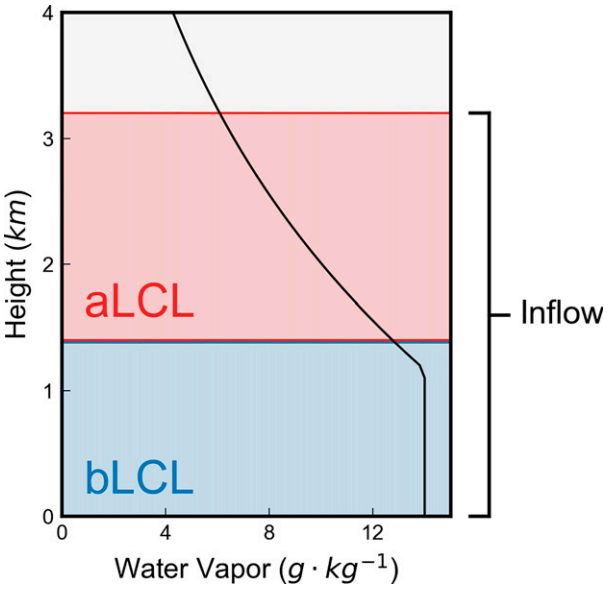

FIG. 2. Vertical profile of water vapor (black curve) at model initialization. Blue box denotes vertical extent of the passive fluid tracer used to define bLCL air, and red box represents that used to define aLCL air. The combined inflow region used to calculate precipitation efficiency (labeled) includes both tracers, and one additional tracer (not shown) centered at the boundary between bLCL and aLCL air to prevent misdiagnosis of undiluted air.

translation as in LT21. The dV/dt term, as well as the horizontal velocity components (u, v) have a star symbol to denote they are storm relative. As before in LT21, w is the vertical component of velocity, ρ is the moist air density, W is the surface area of the core contained in the grid cell, and i, j, and k are grid point indices corresponding to the x, y, and z directions, respectively.

The transition from using ground-relative terms to calculate entrainment as in LT21 to using storm-relative values here in Eq. (1) first requires knowledge of storm updraft coordinates, which can then be used to calculate dV/dt and to derive the storm relative winds. The centroid coordinates of the 5 km AGL, 20 m s^{-1} updraft are recorded at all model output times, and a Savitzky–Golay third-degree polynomial smoothing filter is applied separately on the x and y coordinates over a 21 time step window (Savitzky and Golay 1964). The storm translation vector (i.e., the movement of the supercell core over a single time step) is used to translate the 3D core volume from the previous output time to match the position of the core volume at the current time using the MATLAB function "imtranslate," part of the Image Processing Toolbox. The two 3D core volumes are subtracted (i.e., current volume minus previous) to obtain dV/dt (now representing only the expansion/contraction of the volume), which is then summed with the 3D array containing instantaneous fluxes of air across the core surface, calculated using the storm-relative winds of the current time step. Comparisons of the new and old method for the same simulation showed that estimates of total entrainment agreed within approximately 6%.

d. Diagnosing undiluted air

The Dawe and Austin (2011) entrainment algorithm does not differentiate between the influx of air near the core base that is already within the storm updraft and the entrainment of air into the core aloft, as discussed by LT21. If left unfiltered, this vertical mass flux into the core base leads to an artificial peak of entrainment diagnosed there. Here, two different passive fluid tracers (Fig. 2) are used to discriminate between (i) the vertical flux of air into the core base from below the LCL and (ii) entrainment associated with the storm-relative airstream originating from above the LCL up to approximately 3.2 km AGL altitude. The technique is similar to the passive tracer method used by Nowotarski et al. (2020), but each tracer partially overlaps with the other (by 100 m) to compensate for the effects of numerical diffusion and dispersion which can lead to underestimates of undiluted air. The tracers are replenished at the open-radiative lateral boundaries and are passively advected by the model winds.

The bLCL layer is defined as air originating outside the storm core from 0 to 1.4 km AGL altitude, 200 m thicker than the 1.2 km AGL height of the LCL of the sounding to compensate for the effects of numerical diffusion and dispersion. Being the warmest and moistest air of the sounding, the bLCL air is of interest to track, as it supplies the most buoyancy and moisture to the storm. Undiluted bLCL air is isolated by first locating regions within the 20 m s^{-1} core containing concentrations originating from the lowest tracer exceeding 0.85 kg kg^{-1}. Dilution of this air is then diagnosed through the percentage of the core volume containing undiluted bLCL air. The tracer concentration threshold used in this study (i.e., 0.85 kg kg^{-1}) has been reduced from the 0.99 kg kg^{-1} used in LT21, to account for regions in between adjacent tracers that often have concentrations a little less than 0.99 kg kg^{-1} solely due to numerical diffusion and dispersion instead of physical processes such as entrainment and associated dilution.

e. Isolating entrainment mechanisms

A passive tracer is also used to identify the remaining portion of the storm inflow, previously referred to as the *storm-relative airstream* by LT21, which is considered separately because of its different thermodynamic properties compared to the bLCL air. This air entrained from above the LCL (hereafter aLCL air) is defined using a similar process as the bLCL air but using a tracer spanning 1.4 to 3.2 km AGL in height (red box in Fig. 2). The height of the storm-relative airstream was set to the upper bound of the "effective inflow layer" (Thompson et al. 2007) found in the same sounding by Nowotarski et al. (2020). Three-dimensional visualizations of the tracers (not shown) were used to further validate the technique of isolating these regions. While fluxes of air along the core surface that overlap with bLCL air are not considered entrainment, those corresponding to aLCL air are examined as the storm-relative airstream entrainment mechanism (Fig. 3a). Undiluted aLCL air is again diagnosed as the percentage of the core volume containing these tracers in excess of 0.85 kg kg^{-1}.

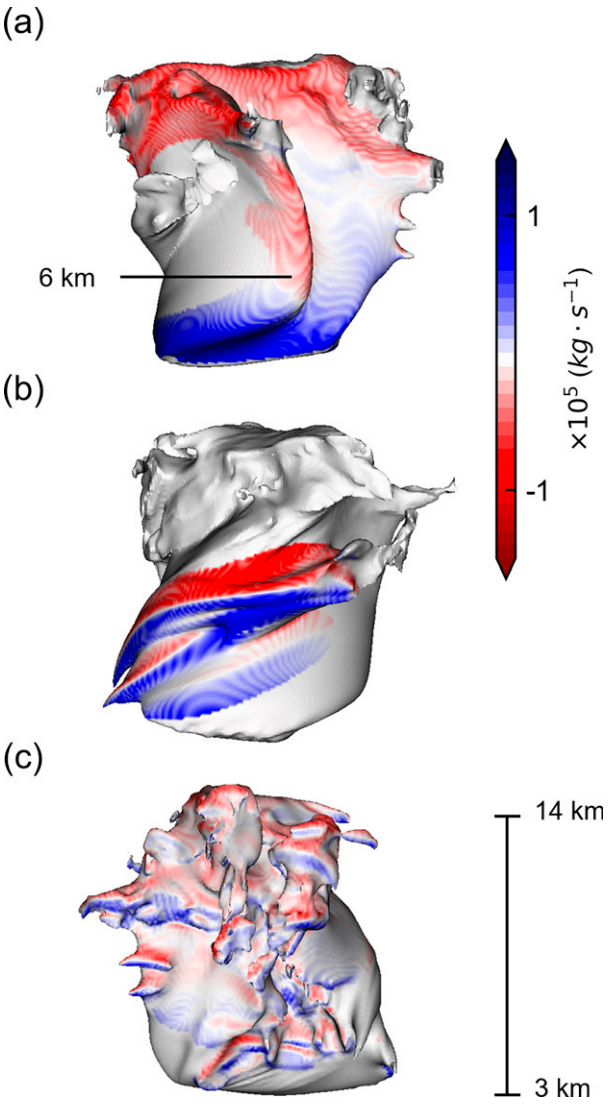

FIG. 3. Three-dimensional view of the 20 m s^{-1} core of the QC120 simulation used in this study. Shaded values of entrainment (blue) and detrainment (red) corresponding to (a) the storm-relative airstream viewed from the east, (b) ribbons viewed from the south, and (c) turbulent eddies viewed from the northwest.

The bLCL and aLCL air are combined in the definition of "storm inflow" later when addressing the issue of precipitation efficiency, due to their shared role in contributing water vapor to precipitation production. The storm inflow is calculated using the tracers defining bLCL and aLCL air, plus an additional tracer centered around the boundary between the two airmasses spanning from 1.2 to 1.6 km AGL (not shown in Fig. 2, but necessary because diffusion in time produces a gap between the aLCL and bLCL regions).

Regions containing the ribbons (Fig. 3b) are identified by contiguous volumes within the core with helicity greater than 3 m s^{-2}, with volumes smaller than 30 grid points (3×10^7 m^3) filtered out to minimize the possibility of capturing small isolated pockets of disintegrating ribbons and other unrelated features such as turbulent eddies. Regions of helicity on the northern half of the core (mostly disorganized turbulent eddies) and those above 10 km AGL height (the turbulent anvil region) are also excluded, unless they are directly connected to the regions of higher helicity within the southwestern quadrant of the core. Finally, this helical region is padded in all directions by 6 grid points (600 m) to fully capture the overturning circulations associated with the ribbons, which contain smaller helicity values at their edges.

Turbulent eddies (Fig. 3c) are isolated using the vorticity magnitude alone; regions that do not correspond to the ribbons but exceed 0.04 s^{-1} of vorticity are isolated and then padded by 4 grid points (400 m) in all directions. The 0.04 s^{-1} threshold is chosen to avoid including other areas of the core that do not correspond to the turbulent eddies, as tested by manual inspection with visualization software, and the padding is applied to include entrainment associated with the same turbulent eddies that falls outside this vorticity threshold.

f. *Quantifying precipitation efficiency*

The condensation efficiency (CE) is a quantity defined here to examine how certain entrainment mechanisms (i.e., ribbons, turbulent eddies) limit condensation and deposition processes within the supercell core. It is meant to approximate how much of the water vapor ingested into the storm core eventually contributes to precipitation production within it, modulated by these entrainment mechanisms. The CE, similar to the definition used by Langhans et al. (2015), is calculated by summing, over time within the analysis period of each storm, both net condensation and net deposition rates within the entire core volume upon the most important hydrometeors there for precipitation production: cloud droplets, raindrops, and graupel.[1] The total rates of condensation and evaporation of water vapor on cloud drops (qc_{cond}, qc_{evap}) and on raindrops (qr_{cond}, qr_{evap}), as well as the deposition and sublimation of water vapor on graupel (qg_{dep}, qg_{sub}) over the entire core are then divided by the rate of net influx of water vapor anywhere across the core surface (qv_{net}):

$$\mathrm{CE} = \frac{qc_{cond} + qr_{cond} + qg_{dep} - qc_{evap} - qr_{evap} - qg_{sub}}{qv_{net}}. \quad (2)$$

All terms on the right-hand side of Eq. (2) are rates, having units of kilograms per second. The value of qv_{net} is calculated using all entrainment and detrainment values along the core surface from the entrainment algorithm including the main updraft through the core base (i.e., bLCL air), and multiplying them by the local water vapor mixing ratio and the moist air density. The CE is designed to be entirely "self-contained" within the storm core.

[1] Microphysical terms corresponding to cloud ice, snow, and hail were excluded in Eq. (2) due to constraints on computational resources, producing underestimations of CE on the order of 5%.

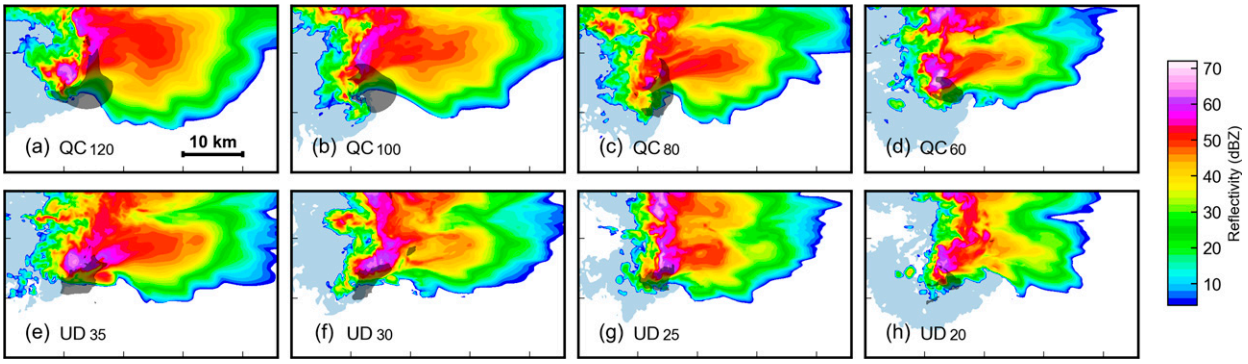

FIG. 4. Simulated radar reflectivity at 1 km AGL height (color bar shown at right), −1-K surface perturbation potential temperature (light blue), and 20+ m s^{-1} updraft at 5 km AGL height (black transparent shading). All plots show cross sections 15 min after the start of the analysis window. Some parts of the unanalyzed anticyclonically rotating storms are apparent near the top of the panels. Length scale is shown in (a).

For comparison, and to relate to historical studies of precipitation efficiency, a more traditional form of precipitation efficiency (PE; e.g., Braham 1952; Auer and Marwitz 1968; Fankhauser 1988) is also calculated by dividing the storm-total surface precipitation rate by only the inflow of vapor into the lower levels of the storm, during the analysis window of each simulation:

$$\mathrm{PE} = \frac{\mathrm{precip}_{\mathrm{surface}}}{\mathrm{qv}_{\mathrm{inflow}}}, \tag{3}$$

where both variables on the right-hand side have units of kilograms per second. Here, $\mathrm{qv}_{\mathrm{inflow}}$ is calculated by using "entrainment" values corresponding to the inflow region (including the bLCL and aLCL air) of the 5 m s^{-1} isosurface surrounding the storm core below 4 km AGL height. These entrainment rates are multiplied by a passive fluid tracer initialized according to the base-state water vapor profile of the sounding (see Fig. 2), and the moist air density. Using this separate tracer allows for a more accurate quantification of the total water vapor ingested into the supercell before it is converted into cloud condensate and/or precipitation, as significant quantities of water vapor are converted into cloud water outside the 5 m s^{-1} updraft. Surface precipitation ($\mathrm{precip}_{\mathrm{surface}}$) of the cyclonically rotating storm was approximated by manually separating it from that of the anticyclonically rotating storm using visual inspection of accumulated surface precipitation as discussed in section 3a. Due to the time lag between the intake of water vapor and surface precipitation (e.g., Fankhauser 1988; Cohen and McCaul 2007), some precipitation would have originated from water vapor ingested before the beginning of the analysis period, and some rainfall produced near the end of the period would not have been considered. Nonetheless, the analysis windows are able to capture the majority of the precipitation produced by the supercells. This form of PE encapsulates the impact of entrainment on precipitation production, as well as the effect of evaporation of falling precipitation, typically enhanced by stronger environmental winds (Marwitz 1972; Foote and Fankhauser 1973; Fankhauser 1988).

3. Results

a. Overview

The simulated storms contain certain features that are characteristic of supercells. The midlevel updrafts increase in width with increasing vertical wind shear (from right to left in each row in Fig. 4) and are often situated near strong low-level hook echoes of simulated radar reflectivity. These supercells are analyzed starting from the time when the cyclonically rotating storm core permanently detaches from the anticyclonically rotating storm core, which is typically characterized by a sharp plunge in the 20 m s^{-1} core volume over a single time step (not shown). The "analysis window" begins at this time for each simulation. As shown in Fig. 5a, the cyclonically rotating supercells in the QC environments translate from west to east in a parabolic arc while those in the UD environments translate in a roughly straight line toward the southeast. The translation speeds of the storms range from 7 to 18 m s^{-1}, mostly proportional to their respective 0–6-km bulk wind shear values (Fig. 5b), consistent with previous studies (Davies and Johns 1993; Bunkers et al. 2000, 2014; Thompson et al. 2007).

The ends of the analysis windows are set to times corresponding to decreases in core volume, decreases in core-top heights (not shown), and/or significant fluctuations in the storm translation vectors—all of which are events that signal fundamental changes in storm dynamics that could significantly skew the relationship of time-averaged properties such as entrainment, CE, and PE versus increasing vertical wind shear. Certain weakly sheared environments produced storms that were more outflow dominant, as seen by the leading edge of the surface cold pool being located ahead of the midlevel updrafts in Figs. 4d, 4g, and 4h. The analysis window is ended before the updraft is fully decoupled from its source of moist air at lower levels within these weakly sheared cases with stronger outflows, and also before the onset of significant mesocyclogenesis in others (Lemon and Doswell 1979; Adlerman et al. 1999; Adlerman and Droegemeier 2005). Such undesirable dynamical changes in supercells can be identified by fluctuations in core volume due to the intermittent

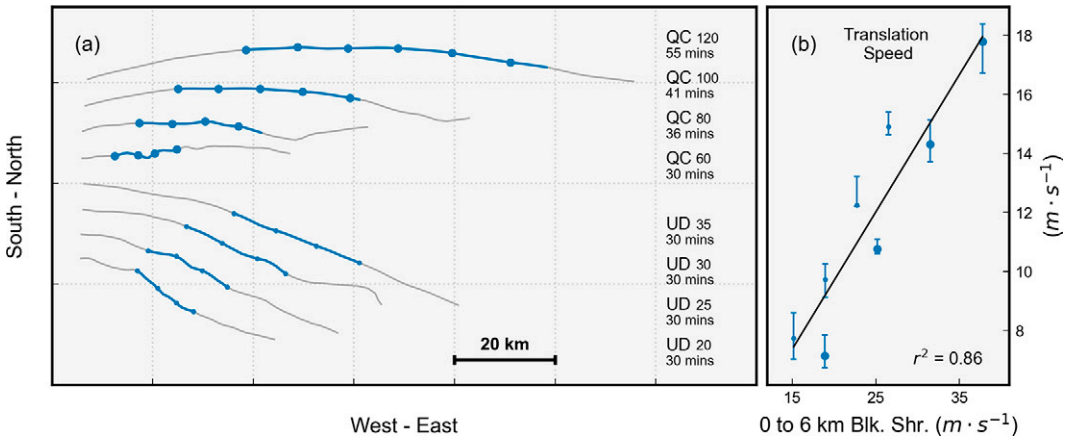

FIG. 5. (a) Cyclonically rotating supercell tracks of the quarter-circle (QC; large dots) and unidirectional (UD; small dots) environments normalized to start at the same point in the east–west direction and spaced apart by 5 km in the north–south direction for clarity. QC tracks are shown from 90 min after model initialization, and UD tracks after 75 min. Gray lines denote the supercell tracks over all model output files and blue lines represent those within the analysis window, with dots spaced apart by 10 min. Legend lists the lengths of the analysis windows. (b) Scatterplot of mean supercell translation speeds vs 0–6-km bulk wind shear. Best-fit line shown in black along with corresponding r^2 value. Dots denote time averages with horizontal bars denoting 25th and 75th percentiles.

detachment of sizable core pieces from the main updraft, along with sharp drops in core-top heights over a short period due to updraft decay (not shown). Supercell cycling behavior can also be detected by significant shifts in storm translation speed and direction, often from new updraft development, which can be seen in the northward transition in the supercell tracks of QC100, QC80, and UD30 shortly after the end of their respective analysis windows in Fig. 5a. Overall, the analysis window lengths increase with vertical wind shear for the QC simulations from 30 to 55 min due to the longer periods that the stronger-shear storms exhibit quasi-steady behavior (based on the metrics discussed above). By contrast, the window lengths remain mostly constant for the UD simulations, at 30 min. All quantities shown for the remainder of this study are evaluated over the entire length of the respective analysis window for each simulation; the varying duration of the analysis periods is necessary to capture the behavior of the supercells over related stages of each simulation.

While the areal extent of surface precipitation in the simulated cyclonically rotating supercells increases with increasing environmental vertical wind shear, the maximum accumulation at any point in that area decreases (Fig. 6, below and to the right of the dotted line). Both effects might be expected from increasing environmental vertical wind shear, with reduced point accumulations due to the increasing storm motions alone (Fig. 5b). Evaluating the entrainment mechanisms in these storms, and understanding their underlying roles in modulating this precipitation, is addressed in the remaining sections. In each panel of Fig. 6, rainfall minima, in the form of a single straight line of the format $y = mx + c$, is used to isolate the precipitation produced by the cyclonically rotating storms from the anticyclonically rotating ones.

In general, the time-averaged total entrainment rates (for all entrainment mechanisms combined over the entire supercell core), increase with increasing vertical wind shear (Fig. 7a), with the supercells in the highest shear environments having entrainment rates more than double those in the lowest shear environments. Fractional entrainment (Fig. 7b), consistent with the findings of Peters et al. (2020), decreases with increasing bulk wind shear, also in accord with past studies (e.g., Kirkpatrick et al. 2009) that found positive relationships between updraft cross-sectional area and vertical wind shear (see Fig. 7d[2]). However, the core surface areas corresponding to entrainment (Fig. 7c) are not as easily related to the environmental shear; there appears to be an inflection point near 25 m s^{-1} of bulk wind shear, beyond which the surface areas of the QC100 and QC120 simulations no longer increase. This influence is also apparent in the total entrainment rates shown in Fig. 7a, and as will be shown shortly, this slower rate of increase in these quantities for the highest shear cases is indicative of a significant shift in the entrainment characteristics within those storms.

b. *Change in specific entrainment mechanisms with increasing vertical wind shear*

In Part I of this study (LT21), three significantly different modes of entrainment were found. The storm-relative airstream, which entrains air containing considerable amounts of water vapor into the core, accounted for 20% of all entrainment in the simulation of LT21. The overturning ribbons, a new entrainment mechanism found by LT21, accounted for 30% of all entrainment. The turbulent eddies accounted for 25% of total entrainment in LT21, corresponding to entrainment associated with high vorticity but not high helicity (i.e.,

[2] The core width is estimated by averaging the maximum and minimum diameters of the convex hull that encloses the core at 5 km AGL height.

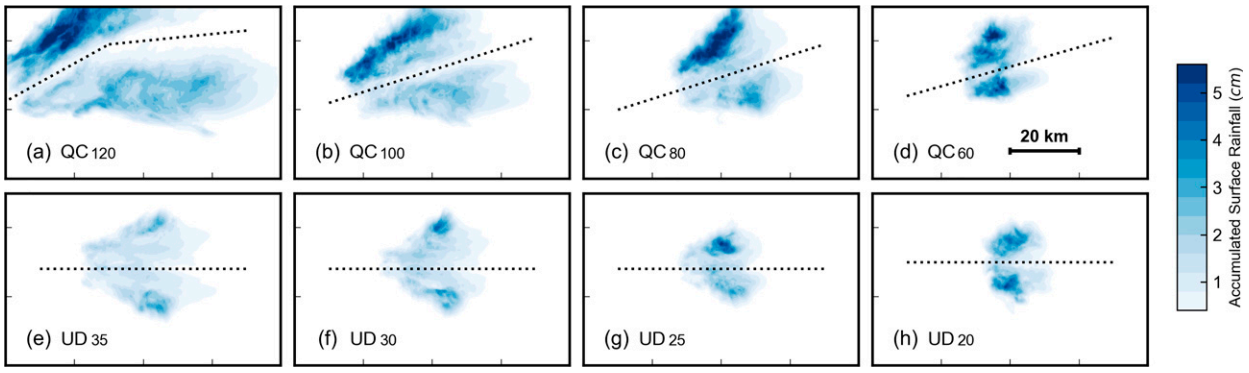

FIG. 6. Shaded accumulated surface precipitation (cm) over the duration of the analysis windows, shown from the ground-relative perspective. Precipitation of both the cyclonically and anticyclonically rotating storms is shown. Black dotted lines denote the boundaries between the precipitation fields; those to the right of and below the line were attributed to the cyclonically rotating storm and thus used in the precipitation efficiency calculations. Length scale is shown in (d).

vortical but unorganized). The remaining 20% of entrainment in LT21 was attributed to the expansion of the core volume (i.e., "engulfment"). For the current study, the engulfment of air by the expansion of the core in any direction has been distributed among the other mechanisms (storm-relative airstream, ribbons, or eddies), as the expansion/contraction of the core would simply add to the air entrained/detrained by each mechanism.

Because LT21 only investigated a single simulation, it was unknown how general the presence of the ribbons might be, but here all eight supercell simulations exhibited these "ribbons," i.e., transient regions of horizontal vorticity that can maintain their circulations for considerable amounts of time. As shown in Figs. 8a–c (also see the animated Fig. S2 of the online supplement), the ribbons translate vertically until each dissipates after reaching the turbulent anvil region, located just above 10 km AGL in height. The characteristic blue–red, entrainment–detrainment couplet corresponding to the ribbons is fully illustrated in Fig. 8d, where diagonal streaks of red and blue are seen translating diagonally over time. The couplet corresponding to ribbon "R1" can be traced for *over 15 min*, but partially extends outside the time frame of Fig. 8d, as the first

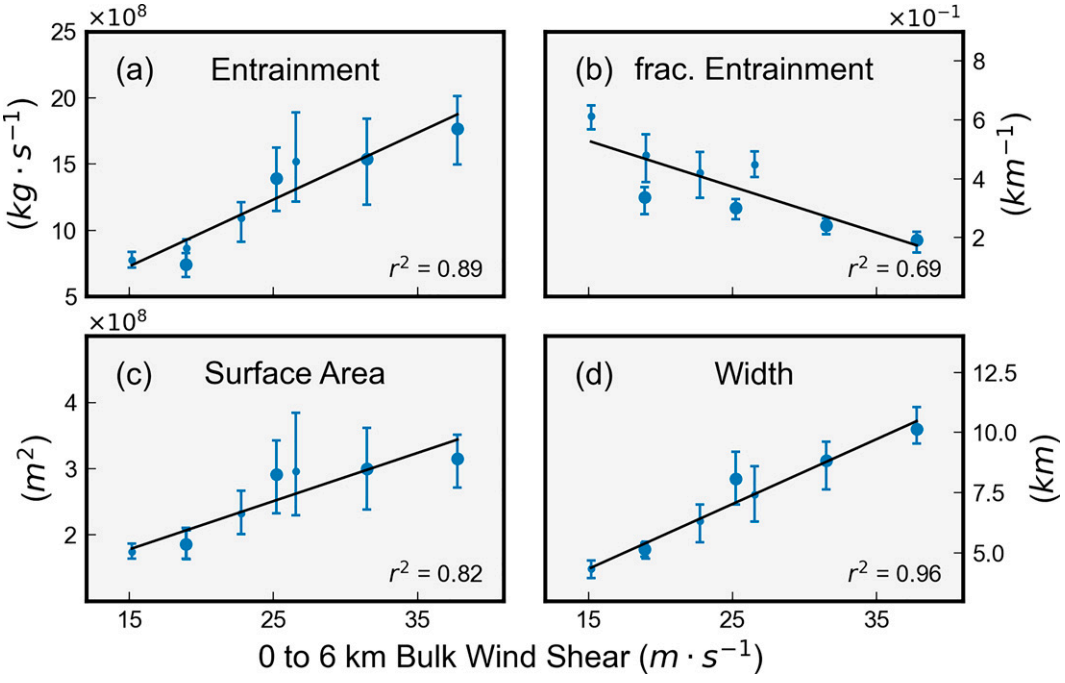

FIG. 7. Scatterplots of time averages over the analysis windows, with the 25th and 75th percentiles shown, of (a) total entrainment rate, (b) fractional entrainment, (c) surface area corresponding to entrainment, and (d) 5 km AGL core width, vs 0–6-km bulk wind shear. Large dots denote values for quarter-circle simulations; small dots denote unidirectional simulations. Black lines correspond to the best-fit lines with r^2 values shown.

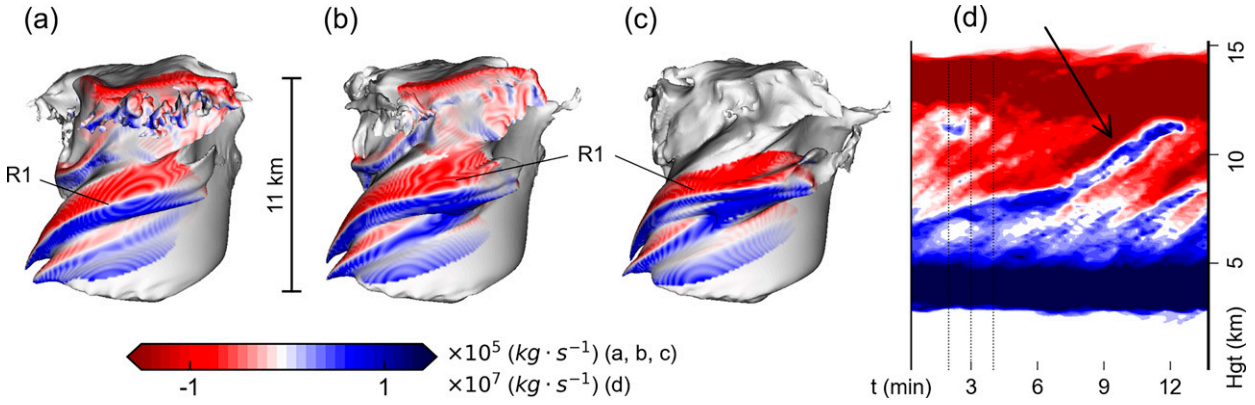

FIG. 8. (a)–(c) Three-dimensional view of the 20 m s^{-1} core of QC120 showing the development of the ribbons over three consecutive minutes. Shaded local values of entrainment (blue) and detrainment (red) correspond to the ribbons. Core is viewed from the south and translates to the right in time. (d) Time–height diagram of net entrainment. Dotted vertical bars in (d) correspond to the times of (a)–(c). Arrow in (d) indicates the entrainment and detrainment couplet corresponding to ribbon R1.

several minutes are before the beginning of the analysis window of this simulation. Ribbons in the simulations with weaker bulk wind shear tended to persist for less time.

The percentage of entrained air over the entire core contributed by the three mechanisms individually changes with environmental vertical wind shear over the eight supercells modeled here (Fig. 9a). The contribution of entrainment by the storm-relative airstream (red symbols) generally increases from 2% to 32% with increasing wind shear. As this entrainment mechanism is largely dependent upon the storm-relative flow influenced by the storm motion, which was found to increase with shear (Fig. 5b), such a result is not surprising. The contribution of entrainment by the ribbons (black symbols) increases from 9% to 25% with increasing wind shear, consistent with the possibility of enhanced vorticity stretching by the stronger storm relative winds. On the other hand, the contribution of entrainment by turbulent eddies (blue symbols) decreases linearly with increasing shear from 85% to 42%.[3] Approximately 1%–4% of the total entrainment could not be clearly assigned to any particular mechanism. As shown in Fig. 9b, the entrainment rate of the turbulent eddies initially increases with increasing vertical wind shear, but then appears to decrease. This decrease appears to result from the turbulent eddies occupying smaller amounts of the core surface area for the simulations having more than 25 m s^{-1} of bulk wind shear; when the entrainment rate is normalized by the surface area over which it is acting, that for the turbulent eddies is still increasing with increasing vertical wind shear (Fig. 7c). On the other hand, the entrainment rates of the aLCL air from the storm-relative airstream, and that from the ribbons, increase nearly linearly with increasing vertical wind shear (Figs. 9b,c). But because the turbulent eddies are the most dominant entrainment mechanism overall (Fig. 9a), their decreasing contribution for the strongest shear simulations (see QC100 and QC120 of Fig. 9b) slows the overall increase in the total entrainment rate (Fig. 7a) and the total surface area over which entrainment is occurring (Fig. 7c).

When the entrainment rates are normalized by the core surface area associated with each mechanism (Fig. 9c), it is also clear that the ribbons have higher local entrainment rates (4.6–6.3 kg m^{-2} s^{-1}) compared to the turbulent eddies (4–5 kg m^{-2} s^{-1}), in accord with the estimates from a single simulation by LT21, but because the ribbons occupy much less of the surface of the storm core, their overall contribution is less (Fig. 9a). The storm-relative airstream has the highest local entrainment rates among the three mechanisms, ranging from 5 to 11 kg m^{-2} s^{-1} (Fig. 9c), and is the most strongly correlated with environmental vertical wind shear. These results are consistent with Warren et al. (2017), who found stronger 0–3-km storm-relative flow and faster storm translation speeds with increasing upper-level vertical wind shear. However, considering that the storm-relative airstream can contribute relatively warmer and moister air to the storm core as opposed to the air entrained by the ribbons and turbulent eddies at higher altitudes, its contribution of up to 32% of entrainment into the core will not be as detrimental to core buoyancy and precipitation.

c. Dilution

As shown in Fig. 7b, fractional entrainment of the simulated supercells decreases with increasing vertical wind shear, consistent with previous studies of ordinary thunderstorms (e.g., De Rooy et al. 2013), squall lines (e.g., Mulholland et al. 2021), and of supercells (LT21; Peters et al. 2020). This trend in fractional entrainment suggests that with increasing vertical wind shear, the supercells are also likely to be less diluted by the ribbons and turbulent eddies discussed in the previous section. However, fractional

[3] In this study, 48% of the entrainment within QC100, the simulation most similar to that analyzed in LT21, is due to turbulent eddies—almost double the value obtained in LT21. Here, the effects of engulfment (i.e., expansion of the core volume) are included in this percentage, and entrainment occurring in the turbulent anvil region was previously ignored in LT21. These changes were made due to their impact on microphysical production rates used later for condensation efficiency.

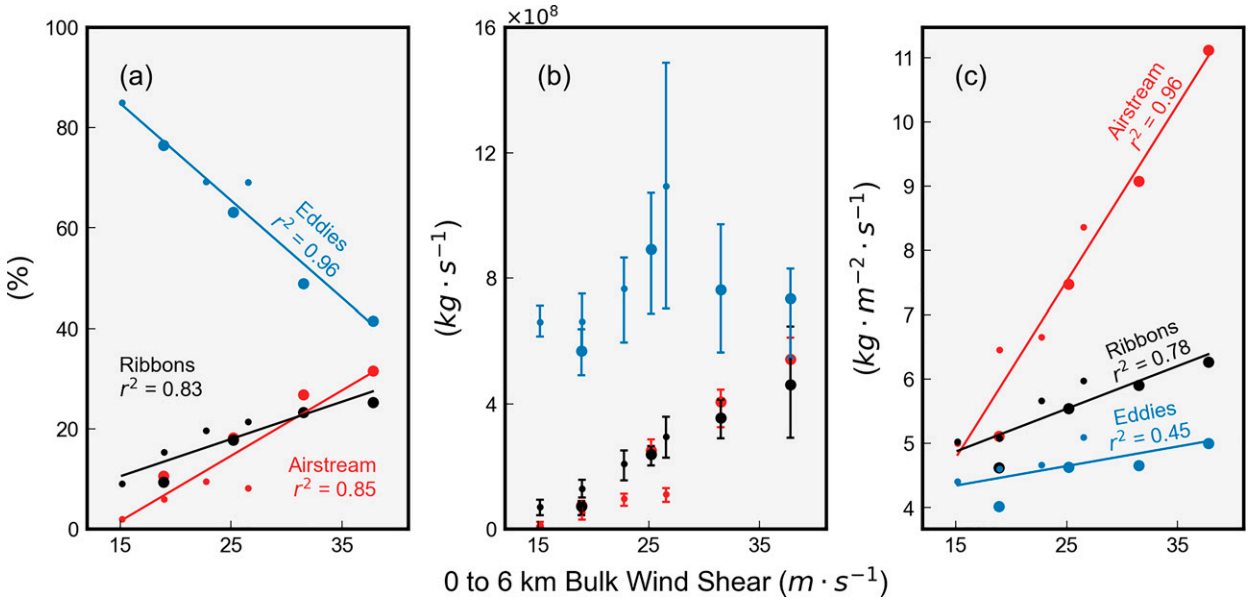

FIG. 9. For individual entrainment mechanisms as labeled: (a) contribution by percentage of time-averaged total entrainment rate, (b) time-averaged entrainment rates, and (c) time-averaged entrainment rates normalized by the surface area over which they are acting. Horizontal bars in (b) denote the 25th and 75th percentiles. Small dots correspond to the unidirectional simulations, while large dots denote the quarter-circle simulations. Best-fit lines and r^2 values are shown in (a) and (c).

entrainment, being essentially a ratio between horizontal to vertical mass fluxes, does not illuminate the subsequent microphysical consequences of entrainment within the core, which also contains significant contributions from the storm-relative airstream, and thus will be explored here.

As shown in Fig. 10, undiluted aLCL air supplied by the storm-relative airstream, which usually occupies different space within the storm core from the undiluted bLCL air, consists of an increasingly larger fraction of the core width (Fig. 11; from 4% to nearly 33%) as the environmental vertical wind shear increases. Thus the storm-relative airstream itself contributes in part to the larger updraft widths with increasing vertical wind shear that has been discussed here (Fig. 7d) and in past studies (Trapp et al. 2017; Peters et al. 2020), and interestingly, helps reduce the "reach" of the entraining eddies and ribbons at the core surface into the core interior, essentially decreasing the effectiveness of their entraining motions in diluting the core. However, the amount of undiluted aLCL air is always less than that of undiluted bLCL air for all the simulations, which increases from 14% to 41%[4] with increasing vertical wind shear (Fig. 11). Because the bLCL air is the warmest and contains the most moisture, those simulations within environments with the greatest shear have much more water vapor to potentially convert into precipitation.

[4] In this study, 40% of the core volume of QC100 consists of undiluted air from the bLCL region. This value is nearly twice that calculated in LT21 due to the different definition of the bLCL tracer, now defined from 0 to 1.4 km AGL instead of from 0 to 1.2 km AGL, and also due to the relaxed definition of undiluted air from 0.99 to 0.85 kg kg^{-1}.

d. Condensation and precipitation efficiencies

The net effect of the entrainment mechanisms on precipitation production within the storm core is approximated using the CE (section 2f). The CE considers condensation, deposition, evaporation, and sublimation rates within the core, including: the undiluted bLCL air, undiluted aLCL air supplied by the storm-relative airstream, the diluted regions of the core affected by the ribbons and turbulent eddies, and any other mixed regions within the core. As the environmental vertical wind shear increases, the CE (Fig. 12a, blue symbols) increases from 63% to 81%. This trend results from the greater increase of the net condensation/deposition rates on cloud water, rain, and graupel (Fig. 12b, blue symbols) as a result of decreased dilution of the (increasing) influx of water vapor into the core (Fig. 12b, red symbols). The storms within highly sheared environments are more efficient at converting water vapor to precipitation within their wider cores, consistent with the increasing fractions of undiluted bLCL and aLCL air with increasing vertical wind shear (Fig. 11) that results from the relatively diminished dilution of the core by the entraining ribbons and eddies.

The increasing CE within the core for increasing environmental vertical wind shear does not translate to the same trends in the traditional form of PE based on the surface rainfall, however. The PE of the simulated supercells (Fig. 12a, red symbols) are calculated by dividing the surface precipitation (Fig. 12c, blue symbols) by the water vapor ingested (Fig. 12c, red symbols) over the analysis window of each simulation. Both quantities increase with increasing vertical wind shear such that the PE values are largely steady, around 20%–30%. Unlike the condensation rates within the core, the

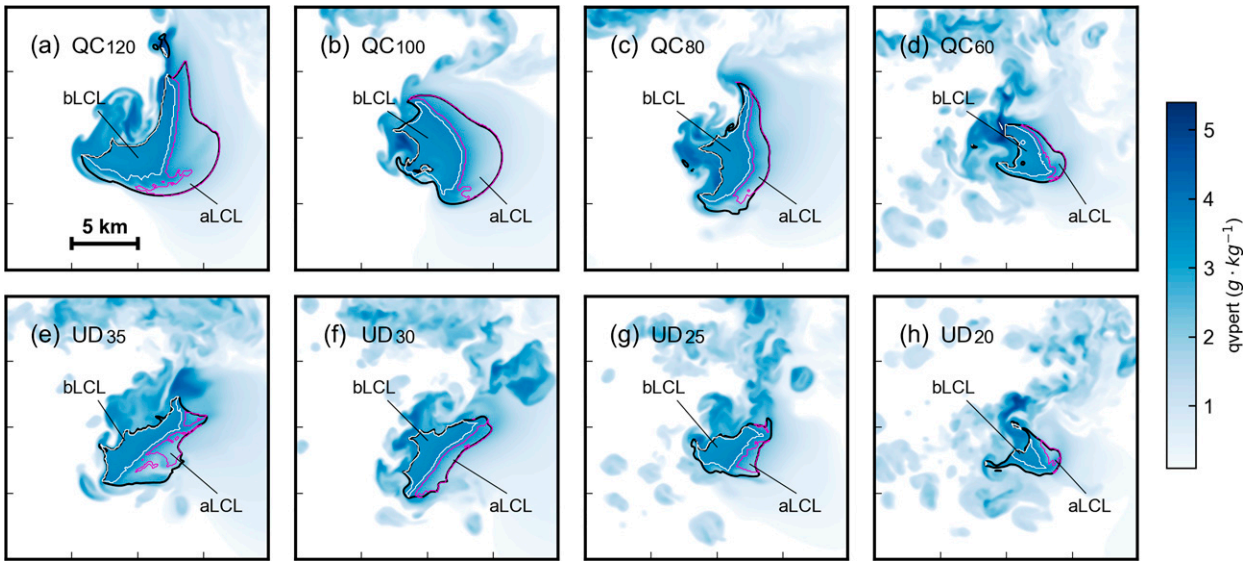

FIG. 10. Horizontal cross sections of water vapor perturbation mixing ratio (i.e., the deviation of water vapor mixing ratio from that of the initial sounding) at 5 km AGL height for all eight simulations. Undiluted bLCL air, enclosed by the white contour, and aLCL air supplied by the storm-relative airstream, enclosed by the magenta contour, are labeled in each panel. The 20 m s^{-1} core is denoted by the black contour. Times corresponding to each simulation are identical to those shown for Fig. 4. Length scale is shown in (a).

surface precipitation is additionally affected by losses due to evaporation and sublimation during its fall toward the surface. Marwitz (1972) proposed that stronger updrafts would loft hydrometeors higher in the storm, and potentially detrain more into the anvil. These hydrometeors would subsequently be carried downwind by the surrounding winds, allowing more depth over which the precipitation could evaporate and/or sublimate before reaching the surface. It was implied in subsequent studies (e.g., Foote and Fankhauser 1973) that this effect could be more pronounced for storms within environments having stronger vertical wind shear (e.g., supercells), where the updrafts are stronger and where the storm-relative winds tend to be greater. The ejection of hydrometeors aloft into the anvil is approximated here by computing the detrainment of undiluted bLCL and aLCL air out of the updraft tops (i.e., above 10 km AGL) normalized by the 5–6 km AGL mean vertical mass flux within the core. This ratio indeed increases with increasing environmental shear (Fig. 13), especially for the QC environments. This trend suggests that the supercells in highly sheared environments are likely to loft *more* precipitation into the upper troposphere, even when scaled for their wider updrafts. The greater amounts of precipitation released into the anvil region would then be advected by the stronger storm relative winds aloft and evaporate and sublimate downstream of the storm core, explaining the overall immense disparity between PE and CE in Fig. 12a, especially for the supercells within the more strongly sheared environments.

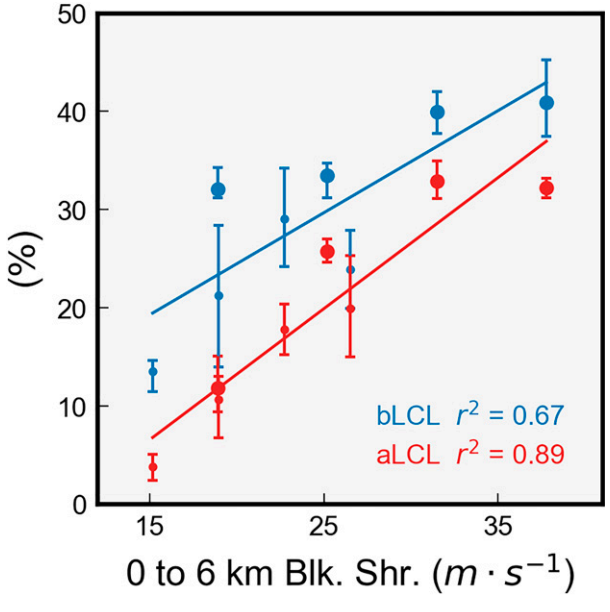

FIG. 11. Time-averaged fraction of core volume (in %) occupied by undiluted bLCL air (blue) and undiluted aLCL air supplied by the storm-relative airstream (red) with the corresponding 25th and 75th percentiles shown, as well as best-fit lines and r^2 values. Smaller dots correspond to unidirectional shear simulations, while larger dots correspond to the quarter-circle shear simulations.

4. Summary and discussion

This study has examined and quantified three different entrainment mechanisms and their general impact on precipitation production, using eight supercell simulations having identical thermodynamic environments but with varying amounts of vertical wind shear. The main findings are as follows:

1) Total entrainment rates into the supercell core updraft increase with increasing environmental vertical wind shear, but less quickly for the highest shear cases. The fractional entrainment rates, more indicative of dilution,

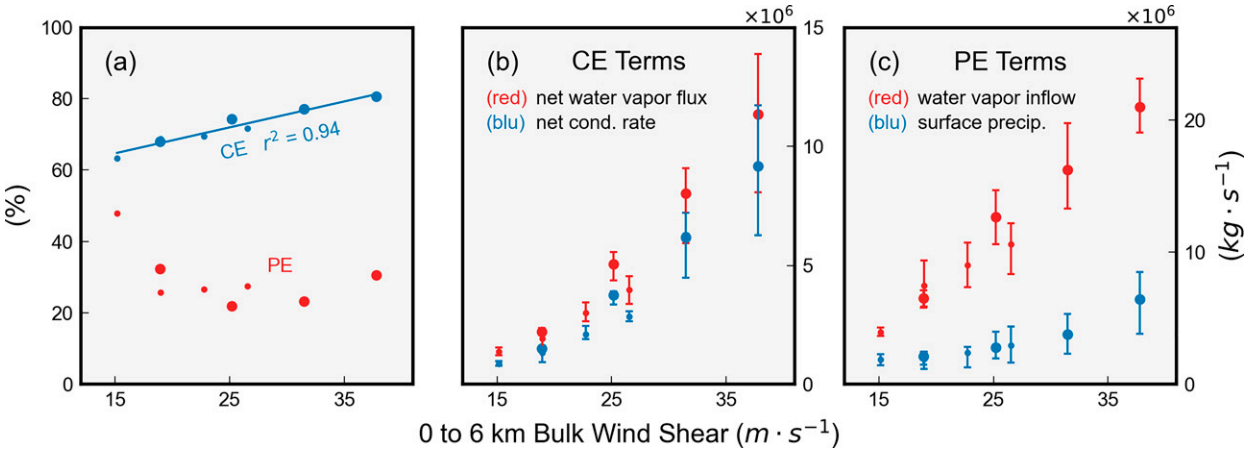

FIG. 12. (a) Condensation efficiency (CE; blue) and precipitation efficiency (PE; red) over the analysis window for each simulation, with the corresponding best-fit line and r^2 value for CE as shown. (b) Net vapor ingested across the core surface (red) and the summed microphysical rates within the core (blue), used to calculate CE, (c) inflow of water vapor (red) and surface precipitation from the right-moving storm (blue), used to calculate PE. Horizontal bars denote the 25th and 75th percentiles. Smaller dots correspond to unidirectional shear simulations and larger dots denote quarter-circle shear simulations; second smaller dot is collocated with first larger dot for the CE shown in (a) and the net condensation rate shown in (b).

decrease with increasing vertical wind shear due to the increasingly wider core widths, as found in past studies.

2) Local entrainment rates for each entrainment mechanism, normalized by the area over which they act, also increase with increasing environmental vertical wind shear. These rates are highest (from 5 to 11 kg m^{-2} s^{-1}) for the storm-relative airstream that introduces air from above the storm base and acts over the smallest surface area of the core. The vertically and cyclonically translating, overturning "ribbons" of horizontal vorticity at the edge of the rotating supercell core locally entrain at rates from 4.6 to 6.3 kg m^{-2} s^{-1}. Disorganized turbulent eddies on the core surface entrain at the lowest rates, from 4 to 5 kg m^{-2} s^{-1}.

3) The contribution of each entrainment mechanism to the total entrainment rate also changes with increasing vertical wind shear. Over the range of environments used here, the contribution from the ribbons increases from 9% to 25%. The contribution from the storm-relative airstream associated with increasing storm translation speeds also increases from 2% to 32%. In contrast, the contribution from the turbulent eddies decreases from 85% to 42%. The contribution from the eddies dominates the total entrainment because of the larger fraction of the core surface area that they occupy, but for the environments with the greatest shear, the rate of increase of this surface area is less, limiting the rate of increase of the overall entrainment for the highest shear cases.

4) Despite the higher entrainment rates that occur with increasing environmental vertical wind shear, the increasingly greater core width limits its dilution, as found in past studies. The amount of the core containing undiluted air from below the LCL increases from 14% to 41%, and that containing undiluted air supplied by the storm relative airstream increases from 4% to 33%.

5) This decreased dilution of the storm core results in a higher efficiency of conversion of water vapor to liquid or ice within the storm core (63%–81%) as the environmental vertical wind shear increases. However, the precipitation efficiency that considers surface rainfall has no clear relationship with vertical wind shear, ranging from 20% to 30%. The increases in vertical wind shear increase detrainment of precipitation out the storm top and its downwind transport, enhancing the evaporation of falling precipitation outside the storm core and decreasing the amount of precipitation reaching the surface. Increases in vertical wind shear also help decrease surface rainfall accumulations at a single location due to faster storm motions.

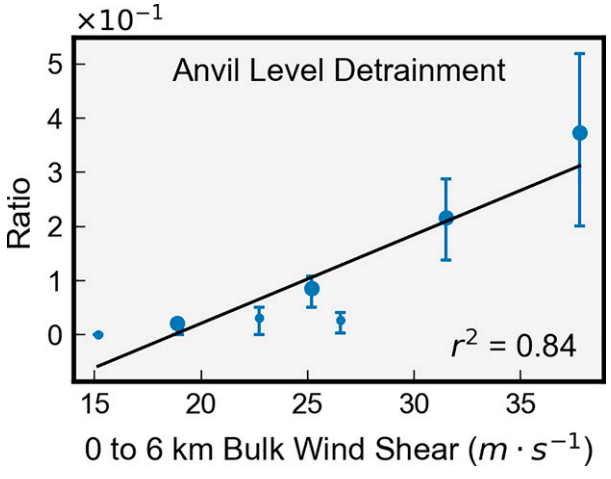

FIG. 13. Time-averaged normalized anvil-level detrainment as explained in main text, with the corresponding best-fit line and r^2 value. Horizontal bars denote the 25th and 75th percentiles. Small dots correspond to the unidirectional simulations and the large dots correspond to the quarter-circle simulations; second smaller dot is collocated with first larger dot.

The generality of these results, while better established than those of LT21 due to the use of eight different simulations of supercells occurring in different sheared environments, still require additional examination, both with numerical modeling and with observations. Further study of supercells within environments with drier vertical humidity profiles than the moist sounding used here may show more dilution. In addition, studying supercells in such environments could clarify trends of the dilutive impact of the ribbons and turbulent eddies not made clear from the simulations here, and may build upon the findings of Grant and Van Den Heever (2014) regarding the dependency of precipitation from supercells upon dry layers in the environment. Observational support for the location, scales, and estimates of entrainment rates, and precipitation efficiency based on surface rainfall, while difficult to obtain, are needed to ensure the numerical results are reasonable. An airborne phased-array radar, capable of observing large areas of the storm core from a nearly horizontal view, holds promise in this regard, as do, to a lesser extent, ground-based mobile radars and enhanced surface mesonets in some regions across the United States.

The results of this study also motivate additional study regarding the nature of turbulence in supercell thunderstorms. Lilly (1986) originally suggested that supercells would be less susceptible to turbulent dissipation due to their helical updrafts, and noted that turbulence would take about twice as long to be established compared to a nonhelical fluid (see also André and LeSieur 1977). While recent studies (e.g., Potvin et al. 2017; Peters et al. 2020) have shown well-developed inertial subranges (i.e., turbulence) for supercell updrafts, the current study has shown that the relationship between the entrainment contributed by turbulent eddies and vertical wind shear is not strictly positive; in fact, the total entrainment by the turbulent eddies and its corresponding surface area was shown here to decrease beyond 25 m s^{-1} of bulk wind shear. When normalized by the surface area over which the eddies were entraining, their entrainment rates did continue to increase with increasing vertical wind shear. This result suggests that supercells in higher-wind-shear environments may have less of the surface area of their rotating updrafts occupied by turbulent eddies. These results, combined with the persistence of the helical ribbons that do not break down for 15 min or more in the highest wind shear case examined here, appear to be somewhat consistent with Lilly's theoretical predictions, but not entirely. Further investigation of the complex relationship between helicity and turbulence in supercell thunderstorms seems warranted.

Acknowledgments. Comments from Professors Robert Trapp, Susan van den Heever, and Ryan Sriver provided useful comments in the planning stages of this study. This study used the open-source CM1 model written and maintained by Dr. George Bryan of the National Center for Atmospheric Research (funded by the National Science Foundation), and the NSSL microphysical parameterization within CM1 written and maintained by Dr. Ted Mansell of the National Severe Storms Laboratory (funded by the National Oceanic and Atmospheric Administration). This study was supported by an award from the National Science Foundation, AGS17-25190, and is also part of the Blue Waters sustained-petascale computing project, which is supported by the National Science Foundation (Awards OCI-0725070 and ACI-1238993), the State of Illinois, and the National Geospatial-Intelligence Agency. Blue Waters is a joint effort of the University of Illinois at Urbana–Champaign and its National Center for Supercomputing Applications.

Data availability statement. The CM1 model is freely available for download at https://www2.mmm.ucar.edu/people/bryan/cm1/. Initialization conditions used to create the numerical simulations for this study can be made available upon request.

REFERENCES

Adlerman, E. J., and K. K. Droegemeier, 2005: The dependence of numerically simulated cyclic mesocyclogenesis upon environmental vertical wind shear. *Mon. Wea. Rev.*, **133**, 3595–3623, https://doi.org/10.1175/MWR3039.1.

——, ——, and R. Davies-Jones, 1999: A numerical simulation of cyclic mesocyclogenesis. *J. Atmos. Sci.*, **56**, 2045–2069, https://doi.org/10.1175/1520-0469(1999)056<2045:ANSOCM>2.0.CO;2.

André, J. C., and M. Lesieur, 1977: Influence of helicity on the evolution of isotropic turbulence at high Reynolds number. *J. Fluid Mech.*, **81**, 187–207, https://doi.org/10.1017/S0022112077001979.

Auer, A. H., Jr., and J. D. Marwitz, 1968: Estimates of air and moisture flux into hailstorms on the High Plains. *J. Appl. Meteor.*, **7**, 196–198, https://doi.org/10.1175/1520-0450(1968)007<0196:EOAAMF>2.0.CO;2.

Barnes, S. L., 1970: Some aspects of a severe, right-moving thunderstorm deduced from mesonetwork rawinsonde observations. *J. Atmos. Sci.*, **27**, 634–648, https://doi.org/10.1175/1520-0469(1970)027<0634:SAOASR>2.0.CO;2.

Braham, R. R., Jr., 1952: The water and energy budgets of the thunderstorm and their relation to thunderstorm development. *J. Atmos. Sci.*, **9**, 227–242, https://doi.org/10.1175/1520-0469(1952)009<0227:TWAEBO>2.0.CO;2.

Bryan, G. H., and J. M. Fritsch, 2002: A benchmark simulation for moist nonhydrostatic numerical models. *Mon. Wea. Rev.*, **130**, 2917–2928, https://doi.org/10.1175/1520-0493(2002)130<2917:ABSFMN>2.0.CO;2.

——, J. C. Wyngaard, and J. M. Fritsch, 2003: Resolution requirements for the simulation of deep moist convection. *Mon. Wea. Rev.*, **131**, 2394–2416, https://doi.org/10.1175/1520-0493(2003)131<2394:RRFTSO>2.0.CO;2.

Bunkers, M. J., B. A. Klimowski, J. W. Zeitler, R. L. Thompson, and M. L. Weisman, 2000: Predicting supercell motion using a new hodograph technique. *Wea. Forecasting*, **15**, 61–79, https://doi.org/10.1175/1520-0434(2000)015<0061:PSMUAN>2.0.CO;2.

——, D. A. Barber, R. L. Thompson, R. Edwards, and J. Garner, 2014: Choosing a universal mean wind for supercell motion prediction. *J. Oper. Meteor.*, **2**, 115–129, https://doi.org/10.15191/nwajom.2014.0211.

Carpenter, R. L., Jr., K. K. Droegemeier, and A. M. Blyth, 1998: Entrainment and detrainment in numerically simulated cumulus congestus clouds. Part I: General results. *J. Atmos. Sci.*, **55**, 3417–3432, https://doi.org/10.1175/1520-0469(1998)055<3417:EADINS>2.0.CO;2.

Cohen, C., and E. W. McCaul Jr., 2007: Further results on the sensitivity of simulated storm precipitation efficiency to environmental temperature. *Mon. Wea. Rev.*, **135**, 1671–1684, https://doi.org/10.1175/MWR3380.1.

Davies, J. M., and R. H. Johns, 1993: Some wind and instability parameters associated with strong and violent tornadoes: 1. Wind shear and helicity. *The Tornado: Its Structure, Dynamics, Prediction, and Hazards*, *Geophys. Monogr.*, Vol. 79, American Geophys. Union, 573–582, https://doi.org/10.1029/GM079p0573.

Davies-Jones, R., 1984: Streamwise vorticity: The origin of updraft rotation in supercell storms. *J. Atmos. Sci.*, **41**, 2991–3006, https://doi.org/10.1175/1520-0469(1984)041<2991:SVTOOU>2.0.CO;2.

——, 2002: Linear and nonlinear propagation of supercell storms. *J. Atmos. Sci.*, **59**, 3178–3205, https://doi.org/10.1175/1520-0469(2003)059<3178:LANPOS>2.0.CO;2.

Dawe, J. T., and P. H. Austin, 2011: Interpolation of LES cloud surfaces for use in direct calculations of entrainment and detrainment. *Mon. Wea. Rev.*, **139**, 444–456, https://doi.org/10.1175/2010MWR3473.1.

De Rooy, W. C., and Coauthors, 2013: Entrainment and detrainment in cumulus convection: An overview. *Quart. J. Roy. Meteor. Soc.*, **139**, 1–19, https://doi.org/10.1002/qj.1959.

Doswell, C. A., III, H. E. Brooks, and R. A. Maddox, 1996: Flash flood forecasting: An ingredients-based methodology. *Wea. Forecasting*, **11**, 560–581, https://doi.org/10.1175/1520-0434(1996)011<0560:FFFAIB>2.0.CO;2.

Fankhauser, J. C., 1988: Estimates of thunderstorm precipitation efficiency from field measurements in CCOPE. *Mon. Wea. Rev.*, **116**, 663–684, https://doi.org/10.1175/1520-0493(1988)116<0663:EOTPEF>2.0.CO;2.

Foote, G. B., and J. C. Fankhauser, 1973: Airflow and moisture budget beneath a northeast Colorado hailstorm. *J. Appl. Meteor. Climatol.*, **12**, 1330–1353, https://doi.org/10.1175/1520-0450(1973)012<1330:AAMBBA>2.0.CO;2.

Fritsch, J. M., and C. F. Chappell, 1980: Numerical prediction of convectively driven mesoscale pressure systems. Part I: Convective parameterization. *J. Atmos. Sci.*, **37**, 1722–1733, https://doi.org/10.1175/1520-0469(1980)037<1722:NPOCDM>2.0.CO;2.

Grant, L. D., and S. C. Van Den Heever, 2014: Microphysical and dynamical characteristics of low-precipitation and classic supercells. *J. Atmos. Sci.*, **71**, 2604–2624, https://doi.org/10.1175/JAS-D-13-0261.1.

Hernandez-Deckers, D., and S. C. Sherwood, 2018: On the role of entrainment in the fate of cumulus thermals. *J. Atmos. Sci.*, **75**, 3911–3924, https://doi.org/10.1175/JAS-D-18-0077.1.

James, R. P., and P. M. Markowski, 2010: A numerical investigation of the effects of dry air aloft on deep convection. *Mon. Wea. Rev.*, **138**, 140–161, https://doi.org/10.1175/2009MWR3018.1.

Jiang, G. S., and C. W. Shu, 1996: Efficient implementation of weighted ENO schemes. *J. Comput. Phys.*, **126**, 202–228, https://doi.org/10.1006/jcph.1996.0130.

Kirkpatrick, C., E. W. McCaul Jr., and C. Cohen, 2009: Variability of updraft and downdraft characteristics in a large parameter space study of convective storms. *Mon. Wea. Rev.*, **137**, 1550–1561, https://doi.org/10.1175/2008MWR2703.1.

Klemp, J. B., and R. B. Wilhelmson, 1978: The simulation of three-dimensional convective storm dynamics. *J. Atmos. Sci.*, **35**, 1070–1096, https://doi.org/10.1175/1520-0469(1978)035<1070:TSOTDC>2.0.CO;2.

Langhans, W., K. Yeo, and D. M. Romps, 2015: Lagrangian investigation of the precipitation efficiency of convective clouds. *J. Atmos. Sci.*, **72**, 1045–1062, https://doi.org/10.1175/JAS-D-14-0159.1.

Lasher-Trapp, S., E. Jo, L. R. Allen, B. N. Engelsen, and R. J. Trapp, 2021: Entrainment in a simulated supercell thunderstorm. Part I: The evolution of different entrainment mechanisms and their dilutive effects. *J. Atmos. Sci.*, **78**, 2725–2740, https://doi.org/10.1175/JAS-D-20-0223.1.

Lebo, Z. J., and H. Morrison, 2015: Effects of horizontal and vertical grid spacing on mixing in simulated squall lines and implications for convective strength and structure. *Mon. Wea. Rev.*, **143**, 4355–4375, https://doi.org/10.1175/MWR-D-15-0154.1.

Lemon, L. R., and C. A. Doswell III, 1979: Severe thunderstorm evolution and mesocyclone structure as related to tornadogenesis. *Mon. Wea. Rev.*, **107**, 1184–1197, https://doi.org/10.1175/1520-0493(1979)107<1184:STEAMS>2.0.CO;2.

Lilly, D. K., 1986: The structure, energetics and propagation of rotating convective storms. Part II: Helicity and storm stabilization. *J. Atmos. Sci.*, **43**, 126–140, https://doi.org/10.1175/1520-0469(1986)043<0126:TSEAPO>2.0.CO;2.

Mansell, E. R., and C. L. Ziegler, 2013: Aerosol effects on simulated storm electrification and precipitation in a two-moment bulk microphysics model. *J. Atmos. Sci.*, **70**, 2032–2050, https://doi.org/10.1175/JAS-D-12-0264.1.

——, ——, and E. C. Bruning, 2010: Simulated electrification of a small thunderstorm with two-moment bulk microphysics. *J. Atmos. Sci.*, **67**, 171–194, https://doi.org/10.1175/2009JAS2965.1.

Marion, G. R., and R. J. Trapp, 2019: The dynamical coupling of convective updrafts, downdrafts, and cold pools in simulated supercell thunderstorms. *J. Geophys. Res. Atmos.*, **124**, 664–683, https://doi.org/10.1029/2018JD029055.

Market, P., S. Allen, R. Scofield, R. Kuligowski, and A. Gruber, 2003: Precipitation efficiency of warm-season Midwestern mesoscale convective systems. *Wea. Forecasting*, **18**, 1273–1285, https://doi.org/10.1175/1520-0434(2003)018<1273:PEOWMM>2.0.CO;2.

Marwitz, J. D., 1972: Precipitation efficiency of thunderstorms on the High Plains. *J. Res. Atmos.*, **6**, 367–370.

Morton, B. R., G. I. Taylor, and J. S. Turner, 1956: Turbulent gravitational convection from maintained and instantaneous sources. *Proc. Roy. Soc. London*, **234A**, 1–23, https://doi.org/10.1098/rspa.1956.0011.

Mulholland, J. P., J. M. Peters, and H. Morrison, 2021: How does vertical wind shear influence entrainment in squall lines? *J. Atmos. Sci.*, **78**, 1931–1946, https://doi.org/10.1175/JAS-D-20-0299.1.

Naylor, J., M. S. Gilmore, R. L. Thompson, R. Edwards, and R. B. Wilhelmson, 2012: Comparison of objective supercell identification techniques using an idealized cloud model. *Mon. Wea. Rev.*, **140**, 2090–2102, https://doi.org/10.1175/MWR-D-11-00209.1.

Newton, C. W., 1963: Dynamics of severe convective storms. *Severe Local Storms*, Amer. Meteor. Soc., 33–58.

Nowotarski, C. J., J. M. Peters, and J. P. Mulholland, 2020: Evaluating the effective inflow layer of simulated supercell updrafts. *Mon. Wea. Rev.*, **148**, 3507–3532, https://doi.org/10.1175/MWR-D-20-0013.1.

Petch, J. C., 2006: Sensitivity studies of developing convection in a cloud-resolving model. *Quart. J. Roy. Meteor. Soc.*, **132**, 345–358, https://doi.org/10.1256/qj.05.71.

Peters, J. M., C. J. Nowotarski, and H. Morrison, 2019: The role of vertical wind shear in modulating maximum supercell updraft velocities. *J. Atmos. Sci.*, **76**, 3169–3189, https://doi.org/10.1175/JAS-D-19-0096.1.

——, ——, and G. L. Mullendore, 2020: Are supercells resistant to entrainment because of their rotation? *J. Atmos. Sci.*, **77**, 1475–1495, https://doi.org/10.1175/JAS-D-19-0316.1.

Potvin, C. K., E. M. Murillo, M. L. Flora, and D. M. Wheatley, 2017: Sensitivity of supercell simulations to initial-condition resolution. *J. Atmos. Sci.*, **74**, 5–26, https://doi.org/10.1175/JAS-D-16-0098.1.

Rio, C., A. D. Del Genio, and F. Hourdin, 2019: Ongoing breakthroughs in convective parameterization. *Curr. Climate Change Rep.*, **5**, 95–111, https://doi.org/10.1007/s40641-019-00127-w.

Rotunno, R., and J. B. Klemp, 1982: The influence of the shear-induced pressure gradient on thunderstorm motion. *Mon. Wea. Rev.*, **110**, 136–151, https://doi.org/10.1175/1520-0493(1982)110<0136:TIOTSI>2.0.CO;2.

——, and ——, 1985: On the rotation and propagation of simulated supercell thunderstorms. *J. Atmos. Sci.*, **42**, 271–292, https://doi.org/10.1175/1520-0469(1985)042<0271:OTRAPO>2.0.CO;2.

Savitzky, A., and M. J. Golay, 1964: Smoothing and differentiation of data by simplified least squares procedures. *Anal. Chem.*, **36**, 1627–1639, https://doi.org/10.1021/ac60214a047.

Simpson, J., R. H. Simpson, D. A. Andrews, and M. A. Eaton, 1965: Experimental cumulus dynamics. *Rev. Geophys.*, **3**, 387–431, https://doi.org/10.1029/RG003i003p00387.

Squires, P., and J. S. Turner, 1962: An entraining jet model for cumulo-nimbus updraughts. *Tellus*, **14**, 422–434, https://doi.org/10.3402/tellusa.v14i4.9569.

Sui, C. H., M. Satoh, and K. Suzuki, 2020: Precipitation efficiency and its role in cloud-radiative feedbacks to climate variability. *J. Meteor. Soc. Japan*, **98**, 261–282, https://doi.org/10.2151/jmsj.2020-024.

Thompson, R. L., C. M. Mead, and R. Edwards, 2007: Effective storm-relative helicity and bulk shear in supercell thunderstorm environments. *Wea. Forecasting*, **22**, 102–115, https://doi.org/10.1175/WAF969.1.

Trapp, R. J., G. R. Marion, and S. W. Nesbitt, 2017: The regulation of tornado intensity by updraft width. *J. Atmos. Sci.*, **74**, 4199–4211, https://doi.org/10.1175/JAS-D-16-0331.1.

Turner, J. S., 1963: The motion of buoyant elements in turbulent surroundings. *J. Fluid Mech.*, **16**, 1–16, https://doi.org/10.1017/S0022112063000549.

Warren, R. A., H. Richter, H. A. Ramsay, S. T. Siems, and M. J. Manton, 2017: Impact of variations in upper-level shear on simulated supercells. *Mon. Wea. Rev.*, **145**, 2659–2681, https://doi.org/10.1175/MWR-D-16-0412.1.

Weisman, M. L., and J. B. Klemp, 1982: The dependence of numerically simulated convective storms on vertical wind shear and buoyancy. *Mon. Wea. Rev.*, **110**, 504–520, https://doi.org/10.1175/1520-0493(1982)110<0504:TDONSC>2.0.CO;2.

——, and R. Rotunno, 2000: The use of vertical wind shear versus helicity in interpreting supercell dynamics. *J. Atmos. Sci.*, **57**, 1452–1472, https://doi.org/10.1175/1520-0469(2000)057<1452:TUOVWS>2.0.CO;2.

Wilhelmson, R. B., and J. B. Klemp, 1978: A numerical study of storm splitting that leads to long-lived storms. *J. Atmos. Sci.*, **35**, 1974–1986, https://doi.org/10.1175/1520-0469(1978)035<1974:ANSOSS>2.0.CO;2.